# Interplay between Chemical Composition and Cation Ordering in the Magnetism of Ni/Fe Layered Double Hydroxides

Gonzalo Abellán,[†] Eugenio Coronado,*,[†] Carlos Martí-Gastaldo,*,[§] Joao Waerenborgh,[‡] and Antonio Ribera[†]

[†]Instituto de Ciencia Molecular (ICMol), Universidad de Valencia, Catedrático José Beltrán 2, 46890 Paterna, Spain
[‡]IST/ITN, Instituto Superior Técnico, Universidade Técnica de Lisboa, CFMC-UL, 2686-953 Sacavém, Portugal
[§]Department of Chemistry, University of Liverpool, Crown Street, L697ZD, Liverpool, U.K.

S *Supporting Information*

ABSTRACT: We report the synthesis of a family of ferrimagnetic NiFe layered double hydroxides (LDHs) with a variable Ni^{2+}/Fe^{3+} in-plane composition of $[Ni_{1-x}Fe_x(OH)_2]\cdot(CO_3)_{x/2}\cdot yH_2O$ (x = 0.20, 0.25, and 0.33) by following a modified homogeneous precipitation. These layered magnets display high crystallinity, homogeneous hexagonal morphologies, and micrometric size that enable their quantitative exfoliation into single layers by sonomechanical treatment of the solids in polar solvents. This was confirmed by dynamic light scattering, UV−vis spectroscopy, high-resolution transmission electron miscroscopy, and atomic force microscopy methodologies to study the resulting steady suspensions. Our magnetic study reflects that the iron content in the LDH layers controls the overall magnetism of these lamellae. Hence, the gradual replacement of Ni^{2+} with Fe^{3+} centers introduces a larger amount of antiferromagnetically coupled Fe−OH−Fe pairs across the layers, provoking that the compound with the highest Fe/Ni ratio displays spontaneous magnetization at higher temperatures (T_{irr} = 15.1 K) and the hardest coercive field (3.6 kG). Mössbauer spectroscopy confirms that the cation distribution in the layers is not random and reflects the occurrence of Fe clustering due to the higher affinity of Fe^{3+} ions to accommodate other homometallic centers in their surroundings. In our opinion, this clarifies the origin of the glassy behavior, also reported for other magnetic LDHs, and points out spin frustration as the most likely cause.
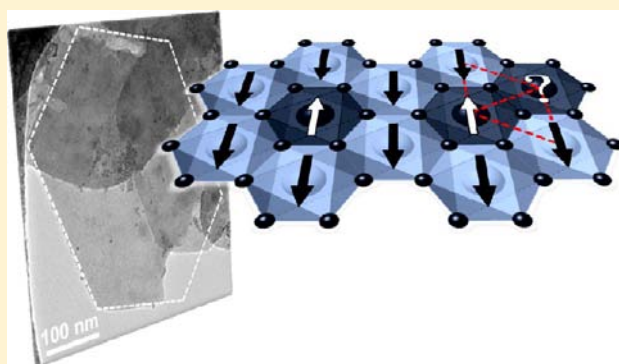
1. INTRODUCTION

Layered double hydroxides (LDHs) are a family of anionic clays that can be formulated as $[M^{II}_{(1-x)}M^{III}_x(OH)_2][A^{n-}_{(x/n)}]\cdot y(H_2O)$, where A^{n-} is the charge compensating anion, and the nature and charge of the components can be varied within a given compositional range ($0.20 \leq x \leq 0.33$) to fix the chemical nature and overall charge of the brucite-like layers.[1,2] The structural flexibility of these layers permits the incorporation of a broad range of organic and inorganic moieties of different natures by anionic exchange, conferring these materials with interesting properties that can be used in diverse fields such as catalysis, medicine, industry, or used as absorbents.[3−13] LDHs incorporating transition metal ions have been also used as precursors for metal oxide-based heterogeneous catalysts as their thermal decomposition leads to the formation of mixed metal oxides that display high metal dispersion and surface area.[2] In addition, the exfoliation of these and related layered hosts in polar solvents to produce unilamellar 2D cationic sheets with nanometric thickness has recently arisen as a versatile approach toward the design of multifunctional layered hybrids that combine the intrinsic properties of the LDH layers with those conferred by other anionic moieties.[14−28]

Notwithstanding their potential interest as magnetic materials, the studies describing the magnetism of LDHs are relatively scarce.[29−33] We previously illustrated how the overall magnetism of these lamellae can be modulated by the interlayer distance and the in-plane chemical composition of the layers in two families of LDHs prepared by the traditional coprecipitation method: $Ni^{II}Fe^{III}$ and $Ni^{II}Cr^{III}$, respectively.[34,35] More recently, O'Hare et al. have described the effect of the particle size and the magnetism for CoAl LDHs synthesized by the reverse micelle method.[36] Although these studies have provided valuable information about the magnetism of these hosts, the true nature of the glassy behavior that is commonly observed at low temperatures has yet to be properly explained. The most likely explanation for this phenomenon relies on the random distribution of metal cations across the layers. In the $Ni^{II}Fe^{III}$ case, for instance, this would combine ferromagnetic Ni−OH−Fe interactions with a residual fraction of antiferromagnetically coupled Fe−OH−Fe pairs to generate spin frustration. However, the ordered or disordered nature of the specific

arrangement of cations in these hydroxide-bridged layers remains still an open debate. Whereas the internal order of Mg^{2+}/Al^{3+} cations in a 2:1 ratio was initially confirmed for MgAl LDHs with sophisticated multinuclear NMR spectroscopic studies,[37] Cadars et al. have recently demonstrated that the occurrence of Al−OH−Al linkages cannot be discarded in these solids because the distribution of cations slightly deviates from perfect order and displays detectable amounts of Al clustering, as confirmed with solid-state NMR and first-principle calculations.[38]

Complementary to these studies centered on diamagnetic hosts, the physical study of magnetic LDHs by introducing Fe^{3+} ions to the layers represents an avenue worth being explored as it can provide further information on the statistical distribution of metal cations across the layers in a family of NiFe-LDHs with variable Ni/Fe ratios. Notwithstanding the synthetic limitations associated with the substitution of Al^{3+} with other trivalent metals, the use of chelating reagents has opened the way to the synthesis of NiFe-LDHs. Here, we report how the use of a slightly modified homogeneous precipitation method that introduces TEA as an auxiliary reagent[39] permits chemical engineering of the in-plane composition of the layers in the $0.20 < x < 0.33$ interval, which maintains the phase purity, morphology, and size of the isolated particles.

$[Ni_{1-x}Fe_x(OH)_2](CO_3)_{x/2} \cdot yH_2O$ with $x = 0.20$ (**1**), 0.25 (**2**), and 0.33 (**3**) has been isolated and magnetically studied. These solids share carbonate as the anion occupying the interlamellar space and display equivalent separation between the magnetic NiFe layers in the layered architectures; therefore, they provide an ideal platform for correlating magnetic behavior and chemical composition. By using Mössbauer spectroscopy, we have extracted direct information on the distribution of the cations across the layers. Additionally, we show how these magnetic clays can undergo quantitative exfoliation upon anion-exchange reactions when suspended in polar solvents. The unilamellar nature and nanometric thickness of the resulting single layers has been unambiguously confirmed by dynamic light scattering (DLS), atomic force microscopy (AFM), and UV−vis spectroscopy.

2. EXPERIMENTAL SECTION

2.1. Synthesis. All Chemicals $Ni(NO_3)_2 \cdot 6H_2O$, $Fe(NO_3)_3 \cdot 9H_2O$, $NaNO_3$, HNO_3, $C_6H_{15}NO_3$ (triethanolamine, TEA), and $CO(NH_2)_2$ (urea) were used as received without further purification. LDHs were synthesized following a modified homogeneous precipitation method by using urea and TEA as an ammonium releasing reagent (ARR) and a chelating agent, respectively. In a typical synthesis of NiFe−CO_3, the nitrate salts of the metals were dissolved in 50 mL of Milli-Q-purged water together with TEA in order to reach a total metal cation concentration of 20 mM in the final solution, varying the stoichiometric coefficient $x = Fe/(Ni + Fe)$ from $x = 0.20$ to $x = 0.33$. The concentration of TEA was varied from one-third to three times the iron concentration. Then, 50 mL of an aqueous solution of urea (35 mM) was added. The amount of urea was fixed at one and three-quarters times the total metal concentration. The resulting dark brown mixture was placed in a 125 mL stainless steel Teflon lined autoclave and heated in an oven. In order to study the effect of thermal treatment on the crystallinity of the final material, the temperature of the oven was set between 125 and 165 °C. After 48 h, the autoclave was cooled on a bench to room temperature, and the resulting yellowish fine powder was filtered, washed thoroughly with Milli-Q water, and dried in a vacuum. The pH value of the remaining solution was around 7.5−8.0.

2.1.1. Anion Exchange. Nitrate exchange was carried out in an excess of nitrate anions. In a typical procedure, 1 g of NiFe−CO_3 LDH

was immersed in a round-bottom flask containing 1 L of an aqueous solution of $NaNO_3$ (1.5 M) and HNO_3 (0.005 M). This mixture was mechanically stirred under inert atmosphere for 48 h. Afterward, the resulting yellowish product was filtered, washed thoroughly with Milli-Q water, and dried in a vacuum at room temperature.

2.1.2. Exfoliation. NiFe−NO_3 was finely powdered and dispersed in degassed formamide at a concentration of 1 g·L^{-1} under inert atmosphere. Then, the mixture was vigorously stirred at 600 rpm for three days. To facilitate the exfoliation, the dispersion was successively sonicated in an ultrasonic water bath (Branson 5510) with three intervals of 20 min during the three days, until the turbidity of the dispersion remained constant. Finally, the yellowish translucent colloidal suspension was centrifuged at 2000 rpm for 10 min to remove the remaining nonexfoliated material. The resulting emulsion clearly exhibited the Tyndall effect when irradiated with a laser beam and was also studied with UV−vis to confirm the presence of exfoliated LDH layers.

2.2. Physical Characterization. The metallic atomic composition of bulk samples was determined by means of electron probe microanalysis (EPMA) performed in a Philips SEM-XL30 equipped with an EDAX microprobe. X-ray powder diffraction patterns were collected with a Siemens d-500 X-ray diffractometer (Cu Kα radiation, $\lambda_\alpha = 1.5418$ Å) equipped with a rotating anode D-max Rigaku operating at 80 mA and 45 kV. Samples were mounted on a flat sample plate with silicon grease. Profiles were collected in the $2.5° < 2\theta < 100°$ range with a step size of 0.05° over a 2.16 h period. The grease is responsible for the broad diffraction observed between 10 and 20°. All patterns have been indexed, and unit cells have been searched with TREOR and refined with the routines implemented in X'Pert HighScore Plus. Particle morphologies and dimensions were studied with a Hitachi S-4800 field emission scanning electron microscope (FESEM) at an accelerating voltage of 20 kV and without metallization of the samples. Infrared spectra were recorded in a FT-IR Nicolet 5700 spectrometer in the 400−4000 cm^{-1} range using powdered samples diluted in KBr pellets. These pellets were prepared just prior to use in order to avoid interference due to anion exchange. UV−vis absorption spectra were recorded using an Agilent 8453 spectrometer in the range from 190 to 900 nm. Thermogravimetric analysis of all compounds was carried out with a Mettler Toledo TGA/SDTA 851 apparatus in the 25−800 °C temperature range under a 10 °C·min^{-1} scan rate and an air flow of 30 mL·min^{-1}. Dynamic light scattering (DLS) measurements were carried out at 25 °C with a Zetasizer Nano ZS instrument (Malvern Instruments, Ltd.) on a freshly prepared solution of exfoliated LDH in formamide (1 g·L^{-1}). Mean hydrodynamic diameter and correlation functions were determined by accumulative analysis. HR-TEM studies of exfoliated nanosheets were carried out on a JEM-2010 microscope (JEOL, Japan) operating at 200 kV. Samples were prepared by dropping a suspension of the fresh exfoliated sample in formamide on a carbon-coated copper grid. The digital analysis of the HR-TEM micrographs was done using a DigitalMicrographTM 1.80.70 for GMS 1.8.0 (Gatan, Inc.). Atomic force microscopy (AFM) measurements were collected in a Multimode atomic force microscope (Veeco Instruments, Inc.). Typically, a freshly diluted emulsion resulting from the exfoliation of NiFe−NO_3 samples in formamide was deposited onto a clean Si wafer by spin coating at 5000 rpm. The images were obtained with a Si tip (frequency and K of ≈300 kHz and 42 N·m^{-1}, respectively) using the tapping-mode in air at room temperature. Images were recorded with 512 × 512 pixel and a 0.5−1 Hz scan rate. Processing and analysis of the images were carried out using the Nanotec WSXM software.

Magnetic susceptibility measurements were performed on polycrystalline samples with a Quantum Design (SQUID) magnetometer MPMS-XL-5. The susceptibility data were corrected by removing the diamagnetic contributions as deduced by using Pascal's constant tables. The dc data were collected in the range of 2−300 K upon decreasing temperatures with an applied field in the range of 100−5000 G, and hysteresis loops were collected between −5 and +5 T at 2 K. Field-cooled (FC) and zero-field-cooled (ZFC) magnetization measurements were performed under a 100 Oe applied magnetic field. The ac data were collected in the range of 2−25 K with an applied alternating

field of 3.95 G at different frequencies in the range of 10−10000 Hz with Quantum Design PPMS-9 equipment.

Mössbauer spectra were collected in transmission mode using a conventional constant-acceleration spectrometer and a 25 mCi ^{57}Co source in a Rh matrix. The velocity scale was calibrated using α-Fe foil. The absorbers were obtained by packing the powdered samples into perspex holders. Isomer shifts are given relative to metallic α-Fe at room temperature. The spectra at 4.1 K were collected using a bath cryostat with the sample immersed in liquid He. The spectra were fitted to Lorentzian lines using a nonlinear least-squares method.[40]

3. RESULTS AND DISCUSSION

3.1. Synthesis of LDHs. Ni^{II}Fe^{III} LDHs were synthesized following a modified homogeneous precipitation by using urea and triethanolamine (TEA) as an ammonium releasing reagent (ARR) and a chelating agent, respectively.[39] In comparison with the traditional coprecipitation methods, the modified homogeneous precipitation route leads to LDH materials with better crystallinity and avoids the so-called "sand rose" morphology, features that are known to limit the efficiency of the exfoliation of these materials. Instead, according to the FESEM (Supporting Information (SI), Figure SI-1) measurements, our solids can be described as irregularly shaped platelets that are 20 nm thick, with lateral sizes ranging from ≈900 to 1700 nm and a remarkable high base-to-height ratio, as highlighted in Figure 1. It is worth outlining that higher [Fe^{3+}] yields bigger particles.
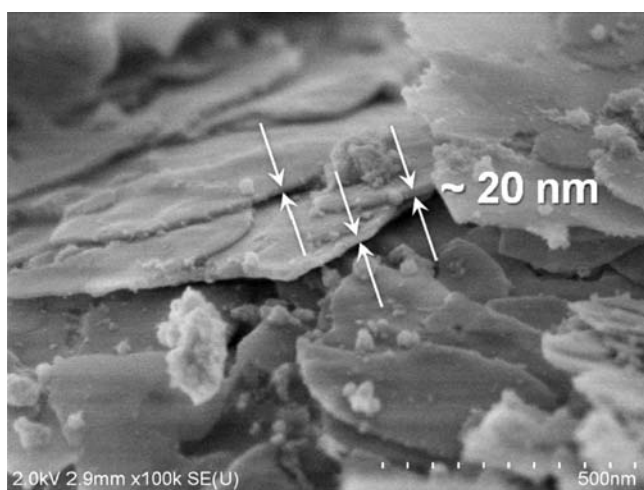
Figure 1. FESEM image of **1**, showing the average thickness of the NiFe LDH crystals.

[Ni$_{1-x}$Fe$_x$(OH)$_2$](CO$_3$)$_{x/2}$·yH$_2$O [x = 0.20 (**1**), 0.25 (**2**), and 0.33 (**3**)] were synthesized under hydrothermal conditions. Here, the ammonia generated by the hydrolysis of urea enables

the progressive increase in the pH of the reaction medium, inducing the slow precipitation of the resulting LDH. To understand the role played by some of these synthetic variables and to define the optimal synthetic conditions needed to isolate pure LDH phases, we have studied the effect played by temperature and [TEA].

Figure SI-2 shows the PXRD patterns of several LDHs obtained from the hydrothermal reaction of a synthetic gel with a fixed metal composition (x = 0.33) at variable temperature between 125 and 165 °C. The highest temperature leads to the residual formation of a spinel phase together with the LDH. The identity of this contaminant phase has been additionally confirmed with magnetic measurements. This is not the case for the samples prepared at lower temperatures in which only pure LDH phases were formed. For the other two compositions studied (x = 0.20 and 0.25), temperature does not drive the formation of contaminant phases within the studied interval. This suggests that the reaction temperature cannot be fixed to a constant value, but it has to be adapted to the metal composition in order to produce pure LDH phases.

Next, we studied the influence of [TEA] between 0.25 and 15 mM (three times the iron concentration) at fixed temperature and composition values of 150 °C and x = 0.25. Figure SI-3 shows how the crystallinity of the formed LDH phase increases with [TEA] up to a maximum at 5 mM. This value corresponds to a 1:1 TEA/Fe^{3+}, supporting the chelating role played by TEA in the reaction that forms stable complexes with the iron ions in solution and avoiding the formation of nonsoluble metallic oxides. This explains why deviations from this [TEA] value leads to poorer crystallinity and broader PXRD patterns, similar to those obtained by traditional coprecipitation methods.

Finally, we carried out anion-exchange reactions to assist the exfoliation of these inorganic layered hosts. The exfoliation of carbonate-intercalated LDHs is unfavorable because of the high charge and small size of CO$_3^{2-}$ that promotes more intense electrostatic interactions in comparison with other monoanions like NO$_3^-$. The nitrate-intercalated compounds were prepared by immersing the starting carbonate LDHs into an aqueous salt−acid mixed solution of NaNO$_3$ and HNO$_3$. Electronic probe microanalysis (EPMA) reflects good agreement between the metal ratios in the LDHs before and after the anion-exchange reaction, thus discarding demetalization of the metal−hydroxide slabs. This information, along with the water content extracted from the thermogravimetric analysis (TGA), was used to calculate the molecular formulas of the samples (see Figure SI-4 and Table 1). As expected for LDHs, higher Fe^{3+} contents lead to more charged LDH layers that require more CO$_3^{2-}$ anions to counterbalance the charge. This promotes a shrinking of the gallery height from more intense electrostatic interaction, thereby decreasing the water content allowed in the inter-

Table 1. Metal Ratio of Synthetic Gels (Calculated) and Isolated Compounds (Experimental) Estimated from Electronic Probe Microanalysis (EPMA), Water Content Deduced from Thermogravimetric Analysis, and Molecular Formulae Calculated for 1−3 (Carbonate Samples)

	x^a		water content		
	calcd	exptl	wt %	mol	molecular formula
1	0.20	0.19	13.1	0.8	[Ni$_{0.81}$Fe$_{0.19}$(OH)$_2$](CO$_3$)$_{0.095}$·0.8H$_2$O
2	0.25	0.25	12.9	0.8	[Ni$_{0.75}$Fe$_{0.25}$(OH)$_2$](CO$_3$)$_{0.125}$·0.8H$_2$O
3	0.33	0.31	8.5	0.5	[Ni$_{0.69}$Fe$_{0.31}$(OH)$_2$](CO$_3$)$_{0.155}$·0.5H$_2$O

$^a x$ = [Fe^{3+}]/([Ni^{2+}] + [Fe^{3+}]).

lamellar space. FESEM images of **4** and **5** confirm that the morphology, thickness, and size of the nanosheets are maintained after the anion-exchange reaction (Figure SI-1).

3.2. Structural Characterization. Figure 2 shows the XRPD patterns of **1**−**3**. They exhibit general structural features
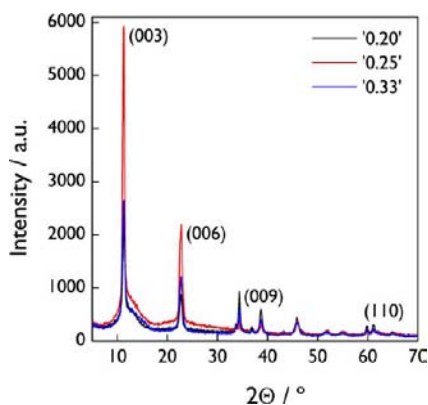
Figure 2. X-ray powder diffraction patterns of **1** (0.20, black), **2** (0.25, red), and **3** (0.33, blue).

of LDH materials with sharp intense peaks at low Θ values and weaker and less defined reflection lines at higher angular values. The diffraction patterns have been indexed and refined by assuming a hexagonal lattice with $R3m$ rhombohedral symmetry, and the calculated cell parameters are summarized in Table 2 and Figures SI-6 and SI-7. The introduction of nitrate upon anion-exchange reactions promotes a negligible increase in the basal space (BS) (Table 2). According to our previous studies, these BS values are slightly lower than those expected for NO_3-intercalated LDHs likely due to the presence of nonexchanged CO_3^{2-} anions.[39] The PXRDs of **4** and **5** display sharp reflection lines and no signature of contaminant phases, confirming that the exchange reaction does not affect the crystallinity of the layered hosts. This is additionally supported by the constant value of the a parameter, which confirms that the internal symmetry of the layers is maintained.

We used FT-IR to monitor the success of the exchange reactions and to confirm the presence of water in the interlamellar space (see Table SI-8). Compounds **4** and **5** show the presence of a weak band centered at 1352 cm^{-1} that can be assigned to the ν_3 stretching mode of CO_3^{2-}. This originates from nonexchanged residual anions and supports the observed deviation in the interlayer distance when compared with the values reported for NO_3-intercalated LDHs.

3.3. Exfoliation. Stable yellowish dispersions of $[Ni_{1-x}Fe_x(OH)_2]^{x+}$ 2D nanosheets were obtained by applying sequential cycles of mechanical stirring and ultrasounds to a suspension of NiFe−NO_3 in formamide $[1\ g \cdot L^{-1}]$. The presence of exfoliated layers was confirmed by the Tyndall light scattering displayed by the dispersion upon irradiation

with a laser beam. Next, the size of the exfoliated layers was studied by DLS. As illustrated in Figure 3, they follow homogeneous Gaussian distributions centered close to 920, 950, and 1770 nm for **4**, **5**, and **6**, respectively, indicating that the size of the nanosheets increases with the $[Fe^{3+}]$ present in the layers. This trend is in excellent agreement with that observed for the size of the particles from the starting LDH-CO_3 (**1**−**3**), as confirmed by the FESEM studies performed on the bulk solids (vide supra).

To confirm the unilamellar nature of the exfoliated nanosheets, we studied the absorption spectra for different concentrations of the as-made colloids at room temperature (Figure 4). The absorption spectra show an intense broad band centered at $\approx$250 nm that can be ascribed to the charge transfer from the hydroxide bridge to the Fe^{3+} ions ($^6A_1 \rightarrow {}^4T_1(P)$),[41] thus confirming the presence of iron in the layers. These bands can be fitted to a linear regime according to the Beer−Lambert law (inset Figure 4), confirming that the dispersions contain a monodisperse distribution of nanosheets, as already reflected by the DLS study.[42]

Figure 5 shows a selection of high-resolution transmission electron micrographs (HR-TEM) of the 2D nanosheets obtained by dropping a freshly prepared dispersion of **4**−**6** on a carbon-coated copper grid. The exfoliated nanosheets show hexagonal morphologies with weak homogeneous contrast, as expected from their nanometric thickness. The selected area electron diffraction (SAED) patterns display a hexagonal arrangement of diffraction spots consistent with the in-plane symmetry of the LDH layers. This confirms that the nanosheets are chemically resilient and can stand the anion-exchange/exfoliation reactions, while maintaining the internal atomic structure of the layers.[17,39]

Figure 6 displays an atomic force microscopy (AFM) image collected by spin coating a dispersion of **6** in formamide on a clean Si wafer. The image confirms the presence of a single nanosheet with an average height profile of 0.75 nm. This value is in excellent agreement with previous reports,[22,39] where the deviation with respect to the crystallographic thickness of a single brucite layer, 0.48 nm, can be ascribed to the physical adsorption of solvent molecules and residual counterions from the dispersion.

3.4. Magnetic Properties. For clarity, it is worthwhile introducing some general aspects of the parameters controlling the magnetism in LDHs. Their overall magnetism is controlled by two main contributions: (a) the intralayer magnetic superexchange between metal centers through the OH bridges across the cationic sheets, and (b) the less intense dipolar interactions operating through the space between the magnetic layers. As the interlayer distance is constant for the samples studied (see Table 2), the change in the magnetic dipolar interactions in the investigated compositional range can be considered small. Hence, the differences in the magnetic behavior can be correlated with variations in the chemical

Table 2. X-ray Diffraction Data and Unit Cell Parameters for 1−3

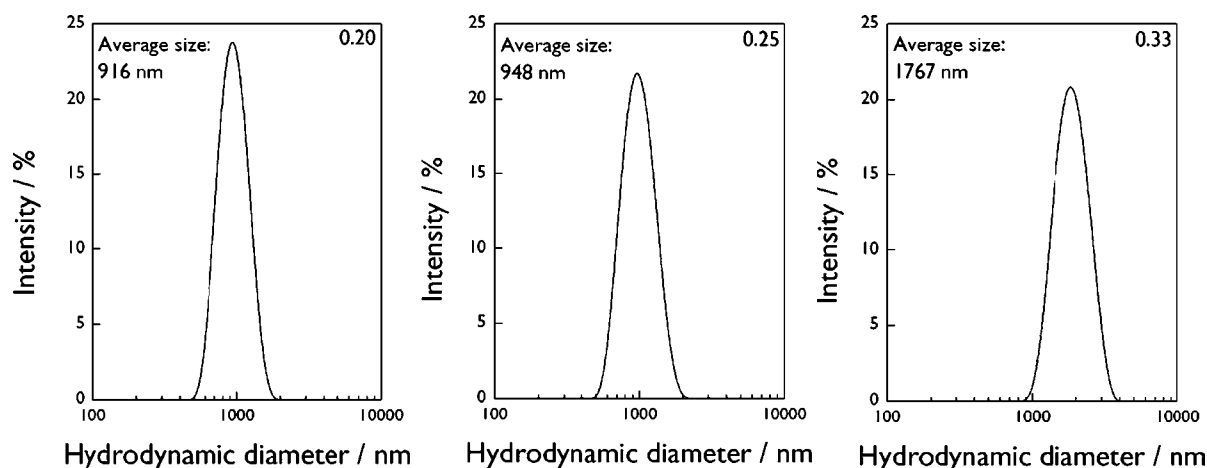|	2Θ [deg] (hkl)				calcd params^a/Å		
	(003)	(006)	(009)	(110)	a	c	BS
1	11.26	22.59	33.69	59.83	3.085(3)	23.48(2)	7.82(7)
2	11.27	22.82	34.27	59.84	3.083(2)	23.34(3)	7.78(1)
3	11.27	22.66	34.34	59.80	3.084(8)	23.5(1)	7.81(8)

^{a}BS = $c/3$.

Figure 3. Distribution of sizes as extracted from DLS studies in the 0.20−0.33 composition range.
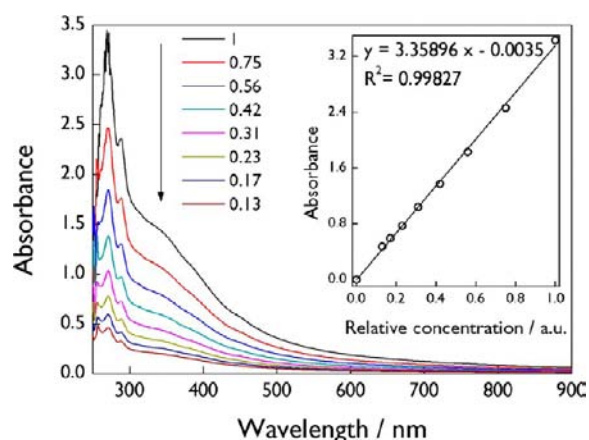

Figure 4. Optical absorption spectra of the colloidal suspension of sample **4** at various relative concentrations. Inset shows the absorbance at 270 nm as a function of the colloid content.

composition. If we assume that the metal cations are statistically distributed across the layers with a ratio imposed by the molecular formula (see the Mössbauer data below), then for a NiFe LDH with a 2:1 metal ratio ($x = 0.33$), each Fe^{3+} ion will be, statistically, surrounded by six Ni^{2+} ions (Ni−OH−Fe pairs), whereas each Ni^{2+} atom will be neighbored by three Fe^{3+} and three Ni^{2+} ions (Ni−OH−Ni and Ni−OH−Fe pairs).[35] Given that the nature of the magnetic superexchange mediated by the −OH bridge changes from ferromagnetic (F) for the coupling between Ni^{2+} centers to antiferromagnetic (AF) when Fe^{3+} cations are involved, variations of the Ni/Fe ratios are expected to cause a change in the relative number of F and AF pairs across the layers, therefore, modifying the overall intralayer structure.

The thermal variation of the product of the molar magnetic susceptibility times the temperature ($\chi_M T$ vs T plot) of **1−3** shows a similar profile (Figure 7a). The $\chi_M T$ remains almost constant upon cooling, down to 50 K, where the signal starts increasing smoothly. From 20 K, this increase becomes more abrupt and defines a maximum for each compound between 5 and 20 K. These maxima correspond to steep jumps in the χ_M signals, suggesting the appearance of a long-range magnetic correlation between the spins at low temperatures (see Figure 7b).

These data were fitted to the Curie−Weiss law in the high-temperature regime (150−300 K, see Figure SI-9), yielding positive Θ values (17.69, 22.57, and 29.11 K) and Curie constants (C) of 2.15, 2.20, and 2.56 emu·K·mol^{-1} for **1**, **2**, and **3**, respectively (see Table 3). Θ shows a gradual increase with the iron content, which likely reflects a higher ferromagnetic contribution to the overall magnetism of these lamellae. C values also increase with the Fe concentration, and they are consistent with those expected for a magnetically diluted combination of noninteracting Ni^{2+} and Fe^{3+} ions with the ratios fixed by the molecular formulas.

Figure 8 displays the field dependence of the initial magnetization of **1−3** at 2 K. They exhibit a sharp increase in the magnetization at very low fields followed by a continuous increase up to 5 T, reaching values of 0.90, 1.01, and 0.76 μ_B for **1**, **2**, and **3**, respectively, that are far from saturation, as expected for ferrimagnetic systems. It is worthwhile outlining that $M(H)$ of **3**, with the highest iron content of the series, displays a sigmoidal shape at low fields, as a result of the increasing AF interactions introduced by the replacement of Ni^{2+} with Fe^{3+}, which might be indicative of metamagnetic behavior. For a better understanding, we measured the field dependence of χ vs T between 100 and 5000 G (see Figure SI-10). Our results discard the presence of a maximum that could be correlated with a field-induced switching of the low-temperature ferromagnetic state into antiferromagnetic, thus ruling out metamagnetism.[43]

Hysteresis loops were recorded for all compounds (Figure 9), confirming the occurrence of spontaneous magnetization at low temperatures. The observed coercive fields (H_{Coer}) of **1** and **2** remain below 1 kG and can be, therefore, classified as soft magnets, whereas **3** is a harder magnet with a H_{Coer} of 3.6 kG (see Table 3). This is likely associated with the higher overall magnetic moment created by the LDH layers as a result of the introduction of Fe^{3+} ions. This results in a more effective anchoring of the magnetic domains in **3** due to more intense ferromagnetic dipolar interactions between neighboring layers.

FC/ZFC measurements permitted extracting the irreversibility temperature values (T_{irr}) for which the onset of spontaneous magnetization is observed in these systems (see Figure 10).[36] As expected from the increasing number of stronger AF interactions, higher iron content triggers an increase of the T_{irr} values from 11.7 K for **1** to 15.1 K for **2** and **3**. Notice that in **1**, the divergence between the FC and the
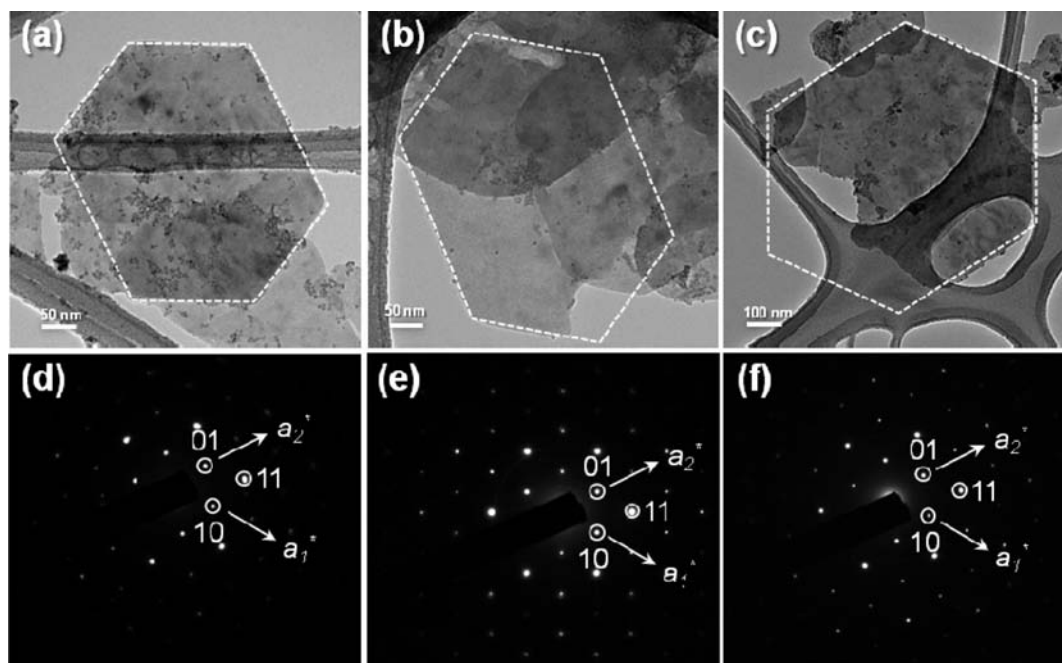
Figure 5. (a−c) HR-TEM images of the exfoliated nanosheets in the 0.20−0.33 compositional range showing their hexagonal morphology. (d−f) SAED exhibiting a hexagonal arrangement of the diffraction peaks, as expected from the intrinsic symmetry of the LDH layers.
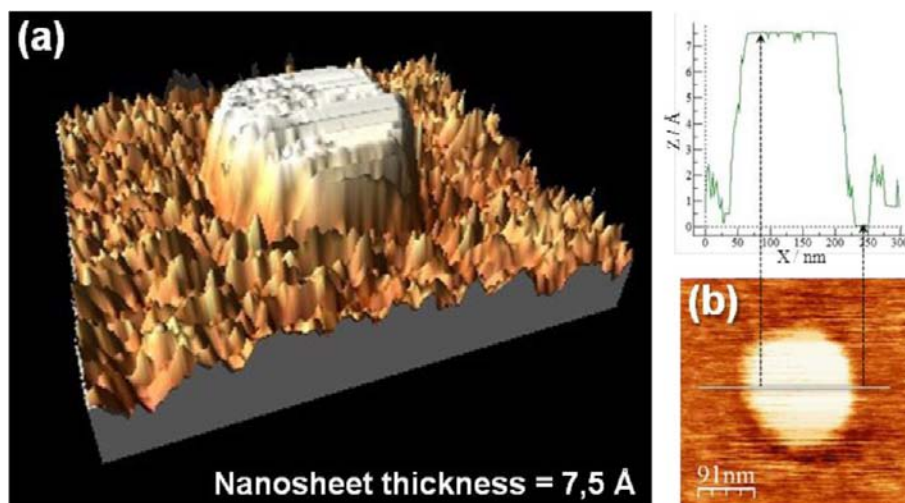

Figure 6. (a) Three-dimensional tapping-mode AFM image (1×1 μm area) of an exfoliated NiFe-LDH nanosheet deposited on a silicon wafer. (b) Height profile concordant with that expected for a single layer (i.e., 0.75 nm).

ZFC curves is rather small, preventing an accurate estimation of T_{irr}.

Spontaneous magnetization at low temperatures was further confirmed with ac dynamic susceptibility measurements in the presence of an external field of 3.95 G, oscillating at different frequencies in the 1−10000 Hz interval. Both the in-phase (χ'_M) and the out-of-phase (χ''_M) signals define a peak at low temperatures. The temperature for the onset of spontaneous magnetization (T_M), defined as the temperature where χ''_M becomes nonzero, falls in the 16−17 K interval for all the solids. Note that the strong frequency dependence exhibited by the ac susceptibility signals hampered an accurate estimate of the T_M values (Figure 11). Below T_M, the χ''_M signal increases very rapidly upon cooling with a negative slope, which is frequency-independent, until reaching a maximum, whose position exhibits a small frequency-dependence.

Equivalent frequency dependence has already been observed in other families of magnetic LDH materials and generally attributed to the presence of spin-glass behavior.[34−36,44−46] Calculation of the frequency shift parameters (ϕ), defined by Mydosh as $\Delta T_{max}/[T_{max}\Delta(\log v)]$, where T_{max} is the freezing temperature and v is the angular frequency, gives 0.025, 0.024, and 0.021 for **1**, **2**, and **3**, respectively. These values are close to those typically observed for canonical spin glasses (0.005−0.018)[47] and in good agreement with previous LDH studies.[34−36,44,46]

Origin of glassiness in this sort of compound is generally ascribed to the coexistence of competing magnetic interactions in the solid. This scenario would result from significant disorder in the distribution of the cations in the layers, thus introducing partial substitution in some of the positions occupied by Ni^{2+} with Fe^{3+} to generate Ni−OH−Fe pairs. This would be more
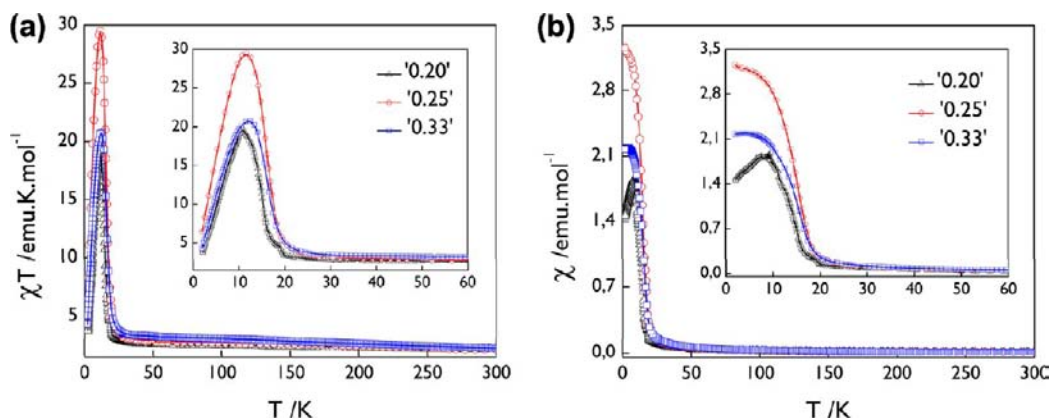
Figure 7. (a) Temperature dependence of the $\chi_M T$ product for **1** (black), **2** (red), and **3** (blue). (b) Represents the χ_M vs T plot. The inset shows the low-temperature regime.
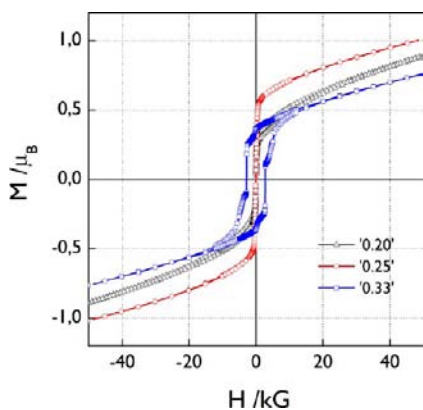
Table 3. Magnetic Parameters for 1−3[a]

sample	C_{so} (emu·K·mol^{-1})	C (emu·K·mol^{-1})	Θ (K)	M_S (50 kG) (μ_B)	H_{Coer} (kG)	T_M (K)	T_{irr} (K)
1 (0.20)	1.64	2.15	17.69	0.90	<1	16.5	11.7
2 (0.25)	2.05	2.20	22.57	1.01	<1	16.7	15.0
3 (0.33)	3.81	2.56	29.11	0.76	3.6	16.8	15.1

[a]Expected spin-only value of the Curie constant [C_{so}, (emu·K·mol^{-1})], experimental Curie constant [C, (emu·K·mol^{-1})], Weiss constant (Θ), saturation magnetization (M_S), coercive field at 2 K (H_{Coer}), temperature of the divergence of the ZFC and FC magnetic susceptibility (T_{irr}), and temperature for the onset of spontaneous magnetization extracted from χ'' plots (T_M). $S(Fe^{3+}) = 5/2$, $S(Ni^{2+}) = 1$.
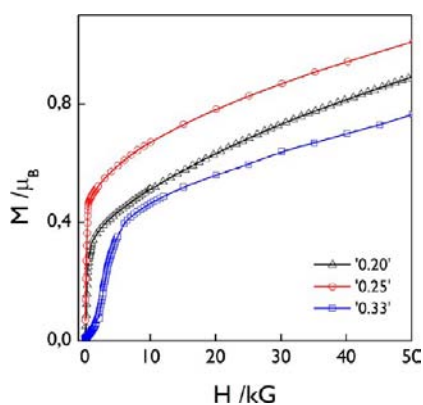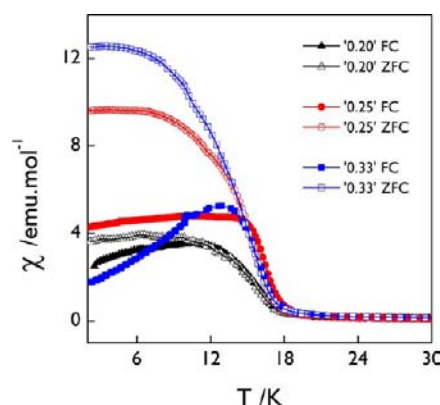

Figure 8. $M(H)$ at 2 K for **1** (black), **2** (red), and **3** (blue).

Figure 10. FC/ZFC measurements for **1** (black), **2** (red), and **3** (blue).

**Figure 9.** Hysteresis loops at 2 K for **1** (black line), **2** (red line), and **3** (blue line).

likely for LDHs with increasing iron content. By assuming that only the nearest-neighbor magnetic interactions are significant,

this substitution would introduce spin frustration to the magnetic layers because of the concurrence of F and AF interactions. This is illustrated in Figure 11d, which shows how this substitution generates spin frustration because the electronic spin of the Ni^{2+} atom is required to be F and AF coupled to the adjacent Ni^{2+} and Fe^{3+} spins simultaneously. To confirm the occurrence of Fe clustering as the origin of the glassy behavior in our materials, we next carried out ^{57}Fe Mössbauer spectroscopy studies to provide definitive information on the local environment of the iron centers.

3.5. Mössbauer Spectroscopy. In agreement with magnetization data, the Mössbauer spectra of **1−3** show paramagnetic behavior at room temperature. At 4 K, the spectra reflect a slowing down of the relaxation of the Fe magnetic moments direction, below the corresponding Larmor precession rate of the ^{57}Fe nuclei, indicating the presence of strong magnetic correlations in the solids.
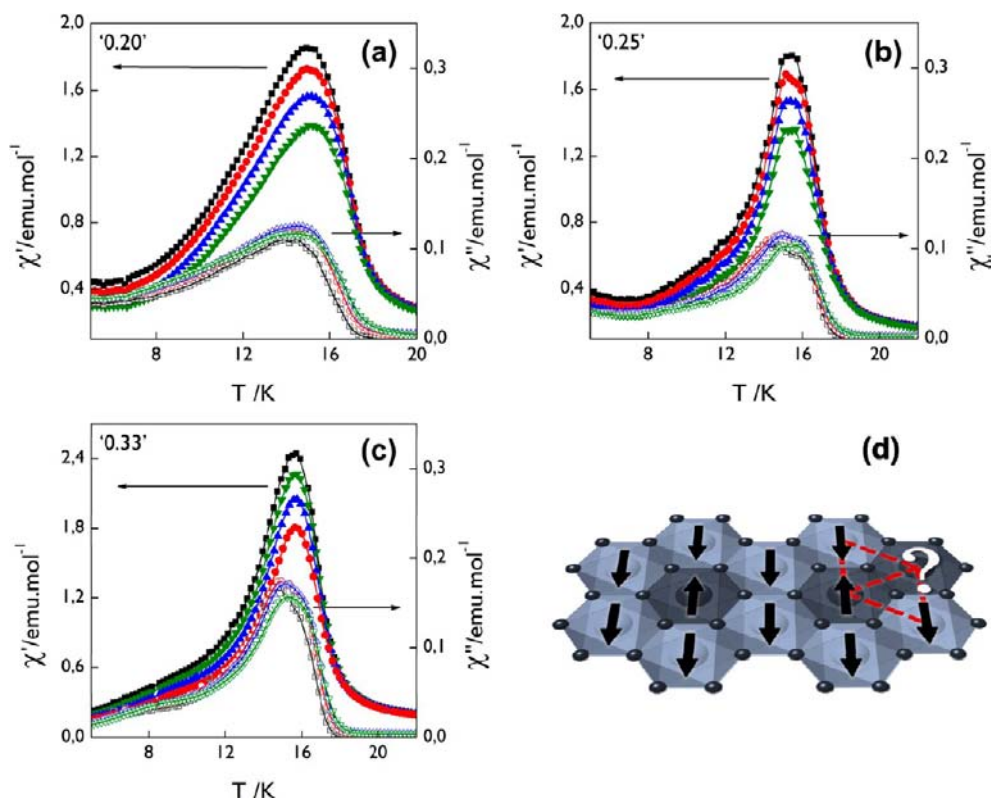
Figure 11. Measurements of ac susceptibility. Solid lines represent in-phase signals, and open symbols represent out-of-phase signals at 10, 100, 1000, and 10000 Hz (black, red, blue, and green data points, respectively, (a–c) correspond to samples **1**, **2**, and **3**, respectively). (d) Schematic representation of the occurrence of spin frustration in the studied compounds.
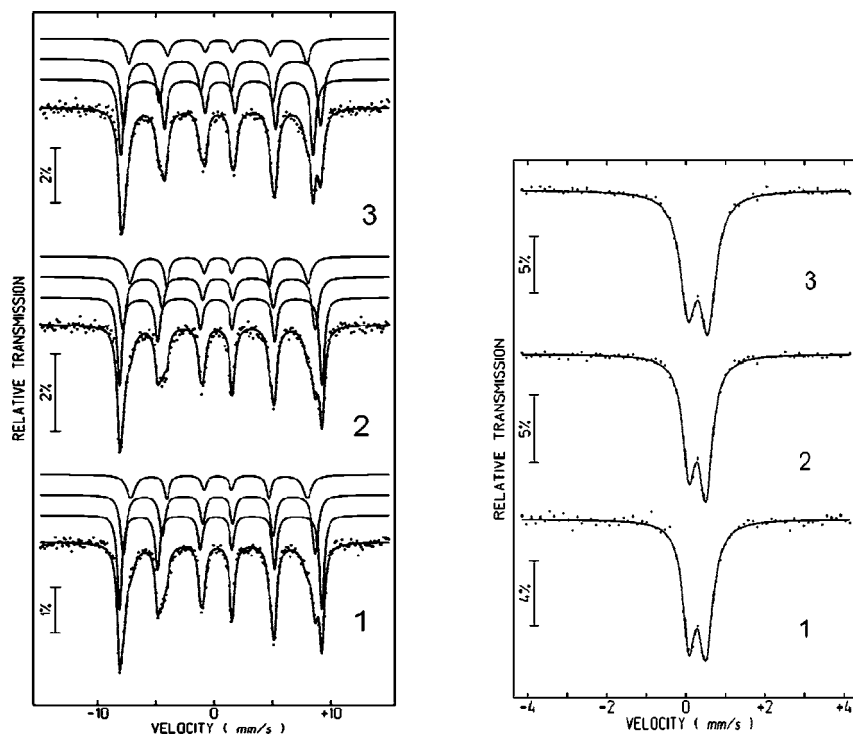
Figure 12. (a) Mössbauer spectra of **1**, **2**, and **3**, collected at 4 K. Lines plotted over the experimental points are the sum of two or three magnetic sextets or magnetic hyperfine field distributions. Subspectra are shown shifted for clarity. (b) Room-temperature Mössbauer spectra.

The spectra of **1** and **2** at 4 K are similar (Figure 12a). They can be fitted with three magnetic sextets, and the estimated parameters are the same within experimental error for both samples (Table 4). Isomer shifts (IS) relative to metallic α-Fe at 295 K and magnetic hyperfine fields (B_{hf}) are typical of high-spin Fe^{III} ($S = 5/2$) octahedrally coordinated by oxygen anions.

Table 4. Estimated Parameters from the Mössbauer Spectra of 1, 2, and 3 Collected at Different Temperatures, T^a

compd	T	IS	QS, ε	B_{hf}	I
		$[Ni^{II}_{0.67}Fe^{III}_{0.33}(OH)_2](CO_3)_{0.165}$ (3)			
3	295 K	0.36	0.52		100%
	4 K	0.51	0.50	52.3	42%
		0.46	−0.26	51.1	40%
		0.45	−0.11	47.1	18%
		$[Ni^{II}_{0.75}Fe^{III}_{0.25}(OH)_2](CO_3)_{0.125}$ (2)			
2	295 K	0.36	0.46		100%
	4 K	0.46	0.38	53.7	43%
		0.45	0.11	51.2	33%
		0.46	0.09	47.2	24%
		$[Ni^{II}_{0.8}Fe^{III}_{0.20}(OH)_2](CO_3)_{0.10}$ (1)			
1	295 K	0.35	0.45		100%
	4 K	0.45	0.38	53.7	42%
		0.46	0.14	51.0	36%
		0.45	0.10	46.8	22%

^{a}IS (mm/s) isomer shift relative to metallic α-Fe at 295 K, QS (mm/s) quadrupole splitting, and ε (mm/s) quadrupole shift estimated for quadrupole doublets and magnetic sextets, respectively. B_{hf} (tesla) magnetic hyperfine field and, I, relative area. Estimated errors ≤0.02 mm/s for IS and QS, < 0.2 T for B_{hf}, and <2% for I.

The spectrum of **3** at 4 K (Figure 12a) may also be fitted with three sextets with IS and B_{hf} similar to those estimated for **1** and **2**, but with quite distinct quadrupole shifts, ε.

This constitutes an initial indication that different nearest-neighbor cation shells are present. In fact, three scenarios are possible: (i) all the Fe^{3+} cations are only surrounded by Ni^{2+} atoms; (ii) there is a random distribution of Ni^{2+} and Fe^{3+}; (iii) the distribution of Ni^{2+} and Fe^{3+} is not ordered, but there is a tendency for Fe^{3+} clustering. In case the of (i), only one sextet should be observed in the Mössbauer spectra because all the Fe^{3+} would have identical environments. Differences in the B_{hf} of Fe^{3+} cations located on the same crystallographic site are frequently observed when more than one kind of cation occupies the same nearest-neighbor positions, leading to different local environments for the Fe^{3+} center.[48,49] This seems to be the case for samples **1**, **2**, and **3**. Since the AF superexchange interactions mediated by the −OH bridge in the resulting Fe−OH−Fe and Fe−OH−Ni pairs are not identical, different B_{hf} values are expected for Fe^{3+} with a different number of Ni^{2+} nearest-neighbors.

The presence of more than one sextet, thus, neglects scenario (i). Still, it remains to be established whether the distribution of the metal cations in the LDH layers is random according to scenario (ii) or is evidence of a tendency for Fe clustering (scenario (iii)). Assuming a completely random occupation by Ni^{2+} and Fe^{3+} of the cation sites in the hydroxide layers, the probability of finding m Ni^{2+} cations in a shell of six nearest-neighbor sites around Fe^{3+} is given by the binomial distribution function

$$P(m) = \frac{6!}{m!(6-m)!}y^m(1-y)^{6-m} \tag{1}$$

where y stands for the fraction of the Ni^{2+} ($y = 0.80, 0.75, 0.67$ for **1**, **2**, and **3**, respectively).

Considering all the Fe^{3+} occupy similar sites (octahedrally coordinated by OH^-), there is no reason to expect that they have significantly different recoil-free fractions. In this case, the relative areas (I) that are estimated from the analyses of the spectra collected at 4 K should be approximately equal to the fraction of Fe^{3+} cations contributing to the corresponding sextets. Therefore, if the metal cations are randomly distributed, the estimated I values should be close to the calculated probabilities $P(m)$ (Table 5). For instance, for compound **1**: $P(6) = 0.262144$ implies that the sextet arising from Fe^{3+} surrounded by 6 Ni^{2+} would have a relative area of $I(6)\sim26\%$, $P(5) = 0.393216$ implies $I(5)\sim39\%$, $P(4) = 0.24576$ implies $I(4)\sim25\%$, and finally, since sextets with $I < 5\%$ with only slightly different IS and B_{hf} are difficult to resolve from the main ones, we might expect that only one more sextet would be clearly observed with an estimated I ($m \leq 3$) approximately equal to the sum of the probabilities for $m = 3, 2, 1$, and 0 ($\sim10\%$). As commented above, the observed differences in B_{hf} values are likely associated with local differences in the Fe^{3+} surroundings due to nonequivalent Fe−OH−Fe and Fe−OH−Ni superexchange interactions. Hence, B_{hf} values are expected to vary monotonically with the progressive substitution of Ni^{2+} with Fe^{3+} cations, thus explaining why the contribution from the unresolved sextets with $I < 5\%$ can be added to those with higher I values and the closest number of Fe^{3+} nearest-neighbors.[48,49] The sets of calculated I values for **1**−**3** that can be correlated with the $P(m)$ values described above for **1** are summarized in Table 6.

Table 6. Sextet Relative Areas Expected for a Completely Random Cation Distribution. $I(m)$ Correspond to the Sextets Arising from Fe^{3+} Cations Surrounded by m Ni^{2+}

compd	$I(6)$	$I(5)$	$I(4)$	$I (m \leq 3)$	
1	26%	39%	25%	10%	
2	18%	36%	30%	16%	
	$I(6)$	$I(5)$	$I(4)$	$I(3)$	$I (m \leq 2)$
3	9%	27%	33%	22%	9%

The sets of experimental I values (Table 4) do not match those calculated, assuming a random distribution of Ni^{2+} and Fe^{3+} (Table 6). Furthermore, while the experimental I values decrease monotonically with B_{hf}, the calculated relative areas for a random distribution of cations display higher I values for intermediate B_{hf} values (Figure SI-11). These differences exclude scenario (ii) indicating that, although not perfectly ordered, the distribution of the metal cations is not completely

Table 5. Probability $P(m)$ of Finding Fe^{3+} Surrounded by m Ni^{2+} Nearest-Neighbors According to the Binomial Distribution (eq 1)

compd	$P(6)$	$P(5)$	$P(4)$	$P(3)$	$P(2)$	$P(1)$	$P(0)$
1	0.262144	0.393216	0.24576	0.08192	0.01536	0.001536	0.000064
2	0.177979	0.355957	0.296631	0.131836	0.032959	0.004395	0.000244
3	0.090458	0.267325	0.329169	0.21617	0.079854	0.015732	0.001291

random either. As referred to above, a perfectly ordered structure would give rise to only one sextet in the spectra. Even if a residual partial substitution of Ni^{2+} by Fe^{3+} occurred, the additional sextets introduced to the overall Mössbauer spectra would have very low relative areas, as compared to the main sextet. This is clearly not the case for the present samples. By assuming that the antiferromagnetic Fe−OH−Fe exchange interactions are stronger and will lead to higher B_{hf} values than the Fe−OH−Ni interactions, B_{hf} is expected to increase with the increasing number of Fe^{3+} nearest-neighbors. The fact that the higher B_{hf} values correspond to experimental I values higher than those calculated by the binomial distribution for the completely random cation distribution, suggest that Fe^{3+} has a higher relative preference for Fe^{3+} nearest-neighbors than for Ni^{2+} nearest-neighbors, in line with the experimental results that confirm the occurrence of Al^{3+} clustering in MgAl LDHs recently reported by Cadars et al.[38] This supports the formation of Fe clusters with the corresponding concurrence of competing F and AF magnetic interactions in the layers, therefore, confirming our previous hypothesis and outlining spin frustration as the most likely cause for the spin-glass behavior observed in magnetic LDHs at low temperatures.

4. CONCLUSIONS

We have isolated and magnetically studied a family of NiFe LDHs with variable Ni^{2+}/Fe^{3+} in-plane composition: $[Ni_{1-x}Fe_x(OH)_2](CO_3)_{x/2}\cdot yH_2O$; $x = 0.20$ (**1**), 0.25 (**2**), and 0.33 (**3**). Notwithstanding the synthetic limitations inherent to replacement of Al^{3+} in the chemistry of LDHs, the use of a modified homogeneous precipitation method enables the formation of highly crystalline, micrometric crystals with hexagonal morphologies for the compositional interval studied, thus discarding the potential magnetic variations associated with variable particle size or heterogeneous morphologies. This homogeneity has also been confirmed at a nanometric scale after exfoliation of these layered hosts into their constituting unilamellar nanosheets by sonomechanical treatment of the solids in polar solvents by the complementary use of DLS, UV−vis, HR-TEM, and AFM. Our study confirms that the exfoliated single layers display equivalent features compared to their bulk counterparts, and the exfoliation does not impose chemical damage or structural variations to the cationic LDH layers.

The reported lamellae provide an ideal scenario for correlating the magnetic behavior of LDHs with chemical composition and cation distribution across the layers, as they share carbonate as the anion occupying the interlamellar space, and they display constant separation between the magnetic NiFe layers in the layered architectures. Magnetic data reflect that **1**−**3** behave as ferrimagnets, as a result of the combined action of F Ni−OH−Ni and AF Ni−OH−Fe and Fe−OH−Fe pairs across the layers and ferromagnetic dipolar interactions operating between layers. The gradual increase in iron content, by replacement of Ni^{2+} with Fe^{3+} centers, enables the appearance of spontaneous magnetization at higher temperatures, as a result of the increasing number of stronger AF interactions across the layers. The introduction of iron also translates into harder magnets with **3**, displaying the highest coercive field of the series.

As previously reported for magnetic LDHs,[34−36,44−46] ac dynamic measurements display frequency dependence that can be associated with spin-glass behavior. By making use of Mössbauer spectroscopy, we demonstrate that the cations are not randomly distributed across the LDH layers and display increasing Fe clustering, that is, the probability for the appearance of AF Fe−OH−Fe pairs, for higher iron contents. This enables the appearance of spin frustration in the layers and confirms this as the origin for glassiness in magnetic LDHs that displays a combination of F and AF pairs.

■ ASSOCIATED CONTENT

Ⓢ Supporting Information

Further details concerning the physical characterization of the materials herein reported: FESEM, XRPD at different temperatures and TEA concentrations, TGA/STDA, metal compositions, FT-IR, additional magnetic measurements, and sextet relative areas estimated from the Mössbauer spectra. This material is available free of charge via the Internet at http://pubs.acs.org.

■ AUTHOR INFORMATION

Corresponding Authors
*E-mail: eugenio.coronado@uv.es (E.C.). Fax: +34 96 354 3273. Tel.: +34 96 354 4415.
*E-mail: gastaldo@liverpool.ac.uk (C.M.). Tel.: +44 (0) 151 794 3711.

Notes
The authors declare no competing financial interest.

■ ACKNOWLEDGMENTS

■ REFERENCES

(1) Cavani, F.; Trifiro, F.; Vaccari, A. *Catal. Today* **1991**, *11*, 173.
(2) Forano, C.; Hibino, T.; Leroux, F.; Taviot-Guého, C. In *Handbook of Clay Science*; Bergaya, F., Theng, B. K. G., Lagaly, G., Eds.; Elsevier: Amsterdam, 2006; Vol. *1*, p 1021.
(3) Rives, V.; Ulibarri, M. A. *Coord. Chem. Rev.* **1999**, *181*, 61.
(4) Choy, J.-H.; Kwak, S.-Y.; Park, J.-S.; Jeong, Y.-J.; Portier, J. *J. Am. Chem. Soc.* **1999**, *121*, 1399.
(5) Leroux, F.; Besse, J.-P. *Chem. Mater.* **2001**, *13*, 3507.
(6) Zhao, M.-Q.; Zhang, Q.; Huang, J.-Q.; Wei, F. *Adv. Funct. Mater.* **2012**, *22*, 675.
(7) Leroux, F.; Taviot-Gueho, C. *J. Mater. Chem.* **2005**, *15*, 3628.
(8) Evans, D. G.; Duan, X. *Chem. Commun.* **2006**, 485.
(9) Liang, J.; Ma, R.; Iyi, N.; Ebina, Y.; Takada, K.; Sasaki, T. *Chem. Mater.* **2010**, *22*, 371.
(10) Yan, D.; Lu, J.; Ma, J.; Wei, M.; Qin, S.; Chen, L.; Evans, D. G.; Duan, X. *J. Mater. Chem.* **2010**, *20*, 5016.
(11) Yao, H.-B.; Fang, H.-Y.; Tan, Z.-H.; Wu, L.-H.; Yu, S.-H. *Angew. Chem., Int. Ed.* **2010**, *49*, 2140.
(12) Li, S.; Lu, J.; Wei, M.; Evans, D. G.; Duan, X. *Adv. Funct. Mater.* **2010**, *20*, 2848.
(13) Shi, W.; He, S.; Wei, M.; Evans, D. G.; Duan, X. *Adv. Funct. Mater.* **2010**, *20*, 3856.
(14) Kaschak, D. M.; Lean, J. T.; Waraksa, C. C.; Saupe, G. B.; Usamiand, H.; Mallouk, T. E. *J. Am. Chem. Soc.* **1999**, *121*, 3435.

(15) Yan, D.; Lu, J.; Wei, M.; Han, J.; Ma, J.; Li, F.; Evans, D. G.; Duan, X. *Angew. Chem., Int. Ed.* **2009**, *48*, 3073.

(16) Yan, D.; Lu, J.; Wei, M.; Ma, J.; Evans, D. G.; Duan, X. *Chem. Commun.* **2009**, 6358.

(17) Liu, Z.; Ma, R.; Osada, M.; Iyi, N.; Ebina, Y.; Takada, K.; Sasaki, T. *J. Am. Chem. Soc.* **2006**, *128*, 4872.

(18) Liu, Z.; Ma, R.; Ebina, Y.; Iyi, N.; Takada, K.; Sasaki, T. *Langmuir* **2007**, *23*, 861.

(19) Adachi-Pagano, M.; Forano, C.; Besse, J.-P. *Chem. Commun.* **2000**, 91.

(20) O'Leary, S.; O'Hare, D.; Seeley, G. *Chem. Commun.* **2002**, 1506.

(21) Li, L.; Ma, R.; Ebina, Y.; Iyi, N.; Sasaki, T. *Chem. Mater.* **2005**, *17*, 4386.

(22) Wu, Q. L.; Olafsen, A.; Vistad, O. B.; Roots, J.; Norby, P. *J. Mater. Chem.* **2005**, *15*, 4695.

(23) Ma, R. Z.; Liu, Z. P.; Li, L.; Iyi, N.; Sasaki, T. *J. Mater. Chem.* **2006**, *16*, 3809.

(24) Hornok, V.; Erdohelyi, A.; Dekany, I. *Colloid Polym. Sci.* **2005**, *283*, 1050.

(25) Szekeres, M.; Szechenyi, A.; Stepan, K.; Haraszti, T.; Dekany, I. *Colloid Polym. Sci.* **2005**, *283*, 937.

(26) Huang, S.; Cen, X.; Peng, H.; Guo, S.; Wang, W.; Liu, T. *J. Phys. Chem. B* **2009**, *113*, 15225.

(27) Han, J. B.; Lu, J.; Wei, M.; Wang, Z. L.; Duan, X. *Chem. Commun.* **2008**, 5188.

(28) Wang, Q.; O'Hare, D. *Chem. Rev.* **2012**, *112*, 4124.

(29) Trujillano, R.; Holgado, M. J.; Pigazo, F.; Rives, V. *Phys. B* **2006**, *373*, 267.

(30) Intissar, M.; Segni, R.; Payen, C.; Besse, J.-P.; Leroux, F. *J. Solid State Chem.* **2002**, *167*, 508.

(31) Bujoli-Doeuff, M.; Force, L.; Gadet, V.; Verdaguer, M.; El Malki, K.; De Roy, A.; Beese, J. P.; Renard, J. P. *Mater. Res. Bull.* **1991**, *26*, 577.

(32) Morlat-Therias, S.; Mousty, C.; Palvadeau, P.; Molinie, P.; Leone, P.; Rouxel, J.; Taviot-Gueho, C.; Ennaqui, A.; de Roy, A.; Besse, J. P. *J. Solid State Chem.* **1999**, *144*, 143.

(33) Giovannelli, F.; Zaghrioui, M.; Autret-Lambert, C.; Delorme, F.; Seron, A.; Chartier, T.; Pignon, B. *Eur. J. Inorg. Chem.* **2008**, 5642.

(34) Almansa, J. J.; Coronado, E.; Marti-Gastaldo, C.; Ribera, A. *Eur. J. Inorg. Chem.* **2008**, 5642.

(35) Coronado, E.; Galan-Mascaros, J. R.; Marti-Gastaldo, C.; Ribera, A.; Palacios, E.; Castro, M.; Burriel, R. *Inorg. Chem.* **2008**, *47*, 9103.

(36) Wang, C. J.; Wu, Y. A.; Jacobs, R. M. J.; Warner, J. H.; Williams, G. R.; O'Hare, D. *Chem. Mater.* **2011**, *23*, 171.

(37) (a) Sideris, P. J.; Nielsen, U. G.; Gan, Z.; Grey, C. P. *Science* **2008**, 113. (b) Sideris, P. J.; Blanc, F.; Gan, Z.; Grey, C. P. *Chem. Mater.* **2012**, *24*, 2449.

(38) Cadars, S.; Layrac, G.; Gérardin, C.; Deschamps, M.; Yates, J. R.; Tichit, D.; Massiot, D. *Chem. Mater.* **2011**, *23*, 2821.

(39) (a) Abellan, G.; Coronado, E.; Marti-Gastaldo, C.; Pinilla-Cienfuegos, E.; Ribera, A. *J. Mater. Chem.* **2010**, *20*, 7451. (b) Han, Y.; Liu, Z.-H.; Yang, Z.; Wang, Z.; Tang, X.; Wang, T.; Fan, L.; Ooi, K. *Chem. Mater.* **2008**, *20*, 360.

(40) Rodrigues, J. V.; Santos, I. C.; Gama, V.; Henriques, R. T.; Waerenborgh, J. C.; Duarte, M. T.; Almeida, M. *J. Chem. Soc., Dalton Trans.* **1994**, 2655.

(41) Bellezza, F.; Nocchetti, M.; Posati, T.; Giovagnoli, S.; Cipiciani, A. *J. Colloid Interface Sci.* **2012**, *376*, 20.

(42) Sasaki, T.; Watanabe, W. *J. Phys. Chem. B* **1997**, *101*, 10159.

(43) Marvilliers, A.; Parsons, S.; Riviere, E.; Audière, J.-P.; Kurmoo, M.; Mallah, T. *Eur. J. Inorg. Chem.* **2001**, 1287.

(44) Abellán, G.; Coronado, E.; Gómez-García, C. J.; Martí-Gastaldo, C.; Ribera, A. *Polyhedron* **2013**, *52*, 216.

(45) Abellán, G.; Busolo, F.; Coronado, E.; Martí-Gastaldo, C.; Ribera, A. *J. Phys. Chem. C* **2012**, *116*, 15756.

(46) Layrac, G.; Tichit, D.; Larionova, J.; Guari, Y.; Guérin, C. *J. Phys. Chem. C* **2011**, *115*, 3263.

(47) Mydosh, J. A. *Spin Glasses: An Experimental Introduction*; Taylor & Francis, Ltd.: London, 1993.

(48) Ferreira, T. A. S.; Waerenborgh, J. C.; Mendonça, M. H. M.; Nunes, M. R.; Costa, F. M. *Solid State Sci.* **2003**, *5*, 383.

(49) Sawatzky, G. A.; van der Woude, F.; Morrish, A. H. *Phys. Rev.* **1969**, *187*, 747.